Surface Science 605 (2011) 1726–1731

Contents lists available at ScienceDirect

Surface Science

journal homepage: www.elsevier.com/ locate/susc

# CO and $H_2O$ adsorption and reaction on Au(310)

M.E. van Reijzen, M.A. van Spronsen, J.C. Docter, L.B.F. Juurlink *

*Leiden Institute of Chemistry, Leiden University, PO BOX 9502, 2300 RA, Leiden, The Netherlands*

ARTICLE INFO

*Article history:*
Received 7 April 2011
Accepted 3 June 2011
Available online 15 June 2011

*Keywords:*
Gold
Carbon monoxide
Water
Surface chemical reaction
Stepped single crystal surface

ABSTRACT

We have studied desorption of $^{13}CO$ and $H_2O$ and desorption and reaction of coadsorbed, $^{13}CO$ and $H_2O$ on Au(310). From the clean surface, CO desorbs mainly in, two peaks centered near 140 and 200 K. A complete analysis of desorption spectra, yields average binding energies of $21 \pm 2$ and $37 \pm 4$ kJ/mol, respectively. Additional desorption states are observed near 95 K and 110 K. Post-adsorption of $H_2O$ displaces part of CO pre-adsorbed at step sites, but does not lead to CO oxidation or significant shifts in binding energies. However, in combination with electron irradiation, $^{13}CO_2$ is formed during $H_2O$ desorption. Results suggest that electron-induced decomposition products of $H_2O$ are sheltered by hydration from direct reaction with CO.



## 1. Introduction

Catalytic activity of gold has been a topic of research since the 1960s [1]. However, it has only attracted significant attention since Haruta's discovery of Au nanoparticles' high activity for CO oxidation [2]. Since this pioneering work, Au nanoparticles have been found to catalyze many more reactions [3–6]. In parallel, surface science studies have investigated the reaction mechanisms underlying gold's remarkable reactivity using well-ordered Au single crystal surfaces. These studies have been reviewed recently [7–10].

The origin of the high catalytic activity of Au nanoparticles toward CO oxidation, and in particular the promotional effect of $H_2O$ on the oxidation rate, are still under debate [11–13]. Based upon catalytic studies of supported Au particles, Daté and Haruta suggested direct reaction of $H_2O$ with $O_2$ yielding OH groups and an activated O atom at the perimeter of nanoparticles as a possible means for $H_2O$ to increase reactivity [11]. Another suggested mechanism was the facilitation of carbonate ($CO_3$) dissociation by water, again accompanied by formation of hydroxyl groups. Recent combinations of density functional theory (DFT) studies and molecular beam experiments [12], near-edge X-ray absorption fine structure (NEXAFS) and infrared (IR) studies [13], and temperature programmed desorption (TPD) and IR studies [14] using a Au(111) single crystal surface show unambiguously that $H_2O$ and surface-bound atomic O form OH groups. These OH groups readily oxidize CO at a surface temperature of 77 K using a CO molecular beam [12]. The reaction is suggested to proceed via an unstable HO–CO intermediate [13].

Although hydroxyl formation from $O + H_2O$ is observed on many other transition metals [15–17] and may be expected to be part of the explanation of gold's capability to oxidize CO at low temperatures, it is not obvious that its occurrence on Au(111) reflects what happens on real catalyst particles. First, such particles are only active in CO oxidation when smaller than 5 nm [3] and at such diameters large (111) domains are not abundant at the catalyst's surface. Second, small particles contain many low coordinated sites, for example at the border between two facets, where the formation of OH from $O + H_2O$ may not occur to a large extent. For two stepped Pt surfaces, we have recently shown that the (111) terraces, (110) steps and (100) steps have strongly varying tendencies to producing OH from coadsorption of $O + H_2O$ [18].

In this article, we investigate the influence of low coordinated Au atoms on coadsorbed CO and $H_2O$. We use the Au(310) surface, which consists of 3-atom wide (100) terraces with monoatomic (110) steps. The surface therefore provides 6-, 8- and 9-fold coordinated atoms, as indicated in Fig. 1a, to interact with adsorbates. We use TPD, Auger electron spectroscopy (AES), and low energy electron diffraction (LEED) in our investigations of adsorption and desorption.

## 2. Experimental

Experiments are carried out using a home-built ultrahigh vacuum (UHV) system with a base pressure of $1 \times 10^{-10}$ mbar during experiments. The UHV chamber and manipulator are constructed for studies of single crystal samples. The chamber is equipped with two quadrupole mass spectrometers (QMS). One QMS (Baltzers, Prisma 200) protrudes into the main chamber and is used for residual gas analysis and angle-integrating TPD spectroscopy. The other QMS (UTI 100c) is differentially pumped and probes desorption of molecules from the sample through a 3 mm diameter opening, positioned ~2 mm away from the face of the

* Corresponding author. Tel.: +31 71 527 4221; fax: +31 84 7182999.
*E-mail address:* l.juurlink@chem.leidenuniv.nl (L.B.F. Juurlink).

0039-6028/$ – see front matter © 2011 Elsevier B.V. All rights reserved.
doi:10.1016/j.susc.2011.06.006

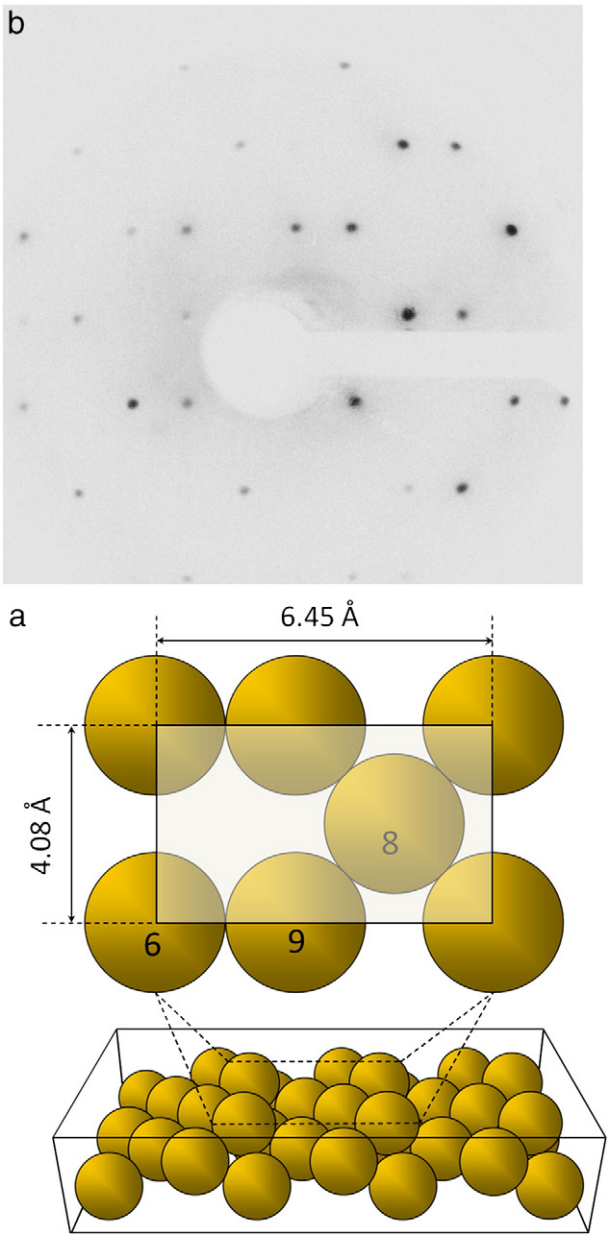


**Fig. 1.** (a) Top and side views of the Au(310) surface with coordination number per Au surface atom type indicated (b) color-inverted LEED image at 190 eV.

sample during TPD measurements. The apparatus also contains equipment to perform LEED (VG RVL 900) and AES (Staib Instruments ESA 100). Finally, it contains two directional dosers that allow for localized gas dosing onto the sample.

For the experiments described here, the sample is a 2 mm thick, 10 mm diameter Au single crystal, cut and polished to within 0.1° of the (310) surface (purity 5 N, Surface Preparation Labs). It is welded at its back edge to a 1 mm wide U-shaped polycrystalline Au ribbon. The ribbon is connected to a small copper block. This block is electrically isolated by aluminum nitride plates from a larger copper arm that connects the sample to the cryostat. The sample may be cooled to approximately 77 K when supercooling the cryostat's $LN_2$ reservoir [19]. For the experiments described here, the crystal is heated radiatively by a filament (Osram, 250 W) mounted behind the sample, although electron bombardment heating is also possible. The crystal temperature is measured by a chromel/alumel thermocouple spot welded to the top edge of the crystal in between the legs of the U-shaped gold ribbon. The thermocouple is electrically decoupled from the PID controller (Eurotherm type 2416) that controls temperature ramps.

The Au(310) surface was daily cleaned by repetitive cycles of $Ar^+$ (5 N) sputtering (5–10 min at 500 V and 2 μA) and 1–5 minute annealing at 860 K. LEED and AES are periodically used to check surface order and cleanliness. Fig. 1b shows a typical LEED image of the cleaned surface, which reflects the exact same spot pattern as observed previously for Ni(310) [20]. The ratio of spot row spacing to spot splitting is consistent with the expected value from an unreconstructed surface (1.58 measured vs. 1.58 calculated) [21]. The only clearly distinguishable peak in our AES spectra up to 1 kV is the Au transition at 69 eV.

For CO adsorption studies, isotopically labeled $^{13}CO$ (MSD isotopes, 99.7% $^{13}C$) was introduced using a leak valve with an elongated nozzle inside the UHV chamber. A short distance between sample and nozzle ensured localized deposition of CO. The sample was flashed to ~280 K prior to CO dosing and kept at 89 K during dosing. Before initiating the TPD ramp, the crystal was cooled to 82 K to ensure linearity in the temperature ramp from 90 K upward. As CO has a high sticking coefficient at the dosing temperature, only a modest increase in background pressure is observed during dosing. Generally, we dose CO with a measured increase in background pressure in the range of $1\times10^{-10}$ to $1\times10^{-9}$ mbar. As the background pressure is on the order of $10^{-10}$ mbar, reproducibility in dosing small amounts of CO was limited.

High purity water (Millipore, R = 18.2 MΩ) was dosed onto the crystal using a home-built capillary array doser [22]. This doser ensures uniform exposure of the single crystal surface to $H_2O$ without significant increase in the background pressure at m/z = 18 in repetitive experiments. The $H_2O$ was degassed by freeze–pump–thaw cycles and kept in a container with He (6 N) at a total pressure of 1.5 bar. The water container was kept at 40°C using a warm water bath to ensure a constant partial pressure of water in the $H_2O$/He mix. Monitoring the pressure rise in the UHV chamber, which results mostly from co-dosed He, allows for reproducible $H_2O$ coverages.

For coadsorption studies, the crystal was flashed to ~280 K, and CO and $H_2O$ were consecutively dosed at a maximum temperature of 89 K. Again, prior to initiating the TPD ramp, the crystal was cooled to 82 K.

Desorption traces were taken at rates of 0.9 $Ks^{-1}$ and 1.8 $Ks^{-1}$. TPD spectra were linear in the range of 90 K to 240 K and were measured using the differentially pumped QMS with an ion energy of 70 V and emission current of 1 mA. TPD traces where recorded with Labview 8.6 based, home-built software and a 12-bit ADAC converter (NI USB-6008).

## 3. Results and discussion

### 3.1. CO desorption from Au(310)

Fig. 2a shows desorption traces of several initial coverages of $^{13}CO$. The TPD traces are characterized by two main features located near 200 K (α) and 140 K ($\beta_1$). The $\beta_1$ feature appears prior to saturation of α. For both features the peak desorption temperature shifts slightly downward with increasing $^{13}CO$ coverage. At the highest doses, a third ($\beta_2$) and fourth ($\beta_3$) feature appear at 110 and 95 K, respectively. LEED images taken at various coverages of $^{13}CO$ show no order other than that of the bare surface (Fig. 1b). The intensity of the spot pattern decreases with CO coverage. The lack of evidence for a particular overlayer structure unfortunately does not allow us to quantify CO adsorption beyond relative values.

Our CO TPD spectra are in good agreement with results published by Weststrate et al. for the same Au(310) surface [23]. They find desorption features near 135 and 185 K in TPD spectra taken at a rate of 5 K $s^{-1}$. In combination with XPS results, they conclude that both TPD features result from step edge desorption. CO desorption from stepped surfaces with 6- and 7-fold coordinated Au atoms is more often found near 190 K

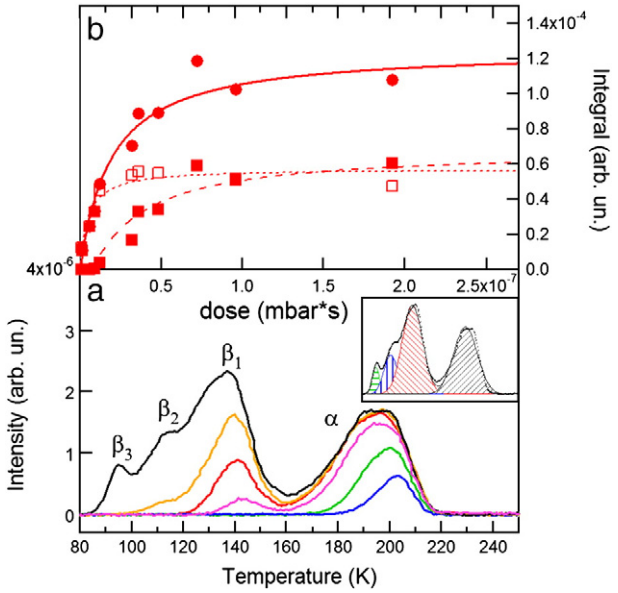


**Fig. 2.** (a) TPD spectra of $^{13}CO$; (inset) example of TPD spectrum deconvolution with original data (dotted) and fits (solid lines and areas); (b) peak integrals as function of dose (for α open squares, for $\beta_1$ solid squares, for total of α and $\beta_1$ closed circles).

and 140 K [23–25]. It is noteworthy that CO desorption from the Au (110)-(1×2) reconstructed surface shows the highest desorption feature around 160 K, dropping continuously with increased CO dose to well below 100 K, even though it also contains 7-fold coordinated Au atoms [26]. Recent DFT-based calculations suggest that only desorption from low coordinated Au atoms is expected above 100 K [27]. We therefore continue our studies with the assumption that the α and $\beta_1$ features result from step edge desorption. The different peak temperatures may result, for example, from two different densities of CO adsorbed at step sites or varying adsorption sites at the step edge. Although any assignment without access to data from other surface sensitive techniques is speculative, we note that the desorption temperature of $\beta_3$ seems consistent with desorption from terrace sites [27].

We have deconvoluted the TPD spectra using Gaussian line shapes. Although this functional form does not properly reflect the time-dependent desorption rate, it provides a reasonably accurate estimate of peak areas, as shown by the example provided as an inset in Fig. 2a. In Fig. 2b, we present the evolution of the α and $\beta_1$ peak areas as a function of $^{13}CO$ exposure. The solid line is a fit to the summed areas of the α and $\beta_1$ peaks using a Langmuir adsorption function for non-dissociative adsorption. It includes data not shown here up to $^{13}CO$ exposure of 12 $10^{-7}$ mbar s. The dotted line is a fit to the data of α using the same functional form. The dashed line equals the difference and nicely fits the $\beta_1$ data. From the fits we can conclude that non-dissociative Langmuirian adsorption describes build-up of $^{13}CO$ with exposure well, and that α and $\beta_1$ are nearly identical in size. The $\beta_2$ and $\beta_3$ features likely give rise to the apparent larger size of $\beta_1$ in comparison to the α feature in TPD spectra. Weststrate et al. based their total adsorption curve on the C1s XPS intensity and fitted it with a linear increase that saturates [23]. This method inherently assumes a coverage-independent sticking probability when averaged over a room temperature kinetic distribution. Our data suggests that this assumption is not correct.

We further analyze our TPD data using a Redhead analysis [28] and by applying a complete desorption rate analysis [29,30] based on the Polanyi–Wigner equation, to α and $\beta_1$:

$$r = -\frac{d\theta}{dt} = \nu(\theta) * \theta^n * e^{-(E_{des}/RT)}$$

The Redhead analysis yields desorption energies, $E_{des}$, of approximately 54 and 37 kJ $mol^{-1}$ for the α and $\beta_1$ features when assuming the same frequency factor as used previously [23]. However, the complete analysis yields different results. For α we have used the original data. To analyze $\beta_1$, α must be subtracted, as well as $\beta_2$ and $\beta_3$ (when present). As these features overlap and the line shapes are not known, indisputable deconvolution is impossible. We have used Gaussian fits as shown in the inset of Fig. 2a, realizing that our results for $\beta_1$ therefore represent no more than a crude estimate of the desorption energy. In Fig. 3 we present the results for α (solid symbols) and $\beta_1$ (open symbols). We have analyzed TPD spectra at multiple coverages relative to saturation of each peak and included all results from spectra taken at 0.9 K/s and 1.8 K/s. For α and $\beta_1$ we find significant scatter in the obtained values of $E_{des}$, but no significant drop with increasing relative coverage. An unconstrained linear fit to the values is nearly flat, which is consistent with only minor reductions of the peak desorption temperatures with varying CO coverage (Fig. 2a). The desorption energy averaged over the whole range of relative coverage for each individual feature is indicated for α and $\beta_1$ as dashed lines. They are found to be $37 \pm 4$ and $21 \pm 2$ kJ $mol^{-1}$, respectively. We have not analyzed $\beta_2$ and $\beta_3$ in a similar fashion as the extent of convolution of these peaks prohibits determining desorption energies with reasonable accuracy.

Table 1 compares our desorption energies to those published previously for the same Au(310) surface by Weststrate et al., which were based on a Redhead analysis of TPD data [23], and binding energies found by Hussain et al. [31], who, from DFT calculations, find the strongest adsorption site for CO to be the 6-fold coordinated Au atom in the step edge. The CO binding energies in Table 1 for the Au (310) surface with its 6-fold coordinated atoms show significant discrepancy, the complete analysis yielding lower values. For adsorption to 7-fold coordinated Au atoms in the (211) [24] and (322) [25] surfaces, binding energies near 50 kJ $mol^{-1}$ have been reported using Redhead analysis of TPD spectra. From DFT studies, CO binding energies for 6-fold coordinated Au atoms have been reported varying from ~35 [32] to ~73 kJ/mol [27,33]. For 7-fold coordinated Au atoms it ranges from 29 [32] to 63 kJ $mol^{-1}$[27]. It seems that there is no consensus yet from either theoretical or experimental studies on the binding energy for CO to low coordinated Au atoms. Our results indicate that care must be taken in the type of analysis used to extract desorption energies from experimental data.

### 3.2. $H_2O$ desorption from Au(310)

Fig. 4 shows TPD spectra of water desorbing from the bare Au(310) surface. It is noteworthy that we observe desorption in two separate peaks. The earliest studies of water desorption from a gold single

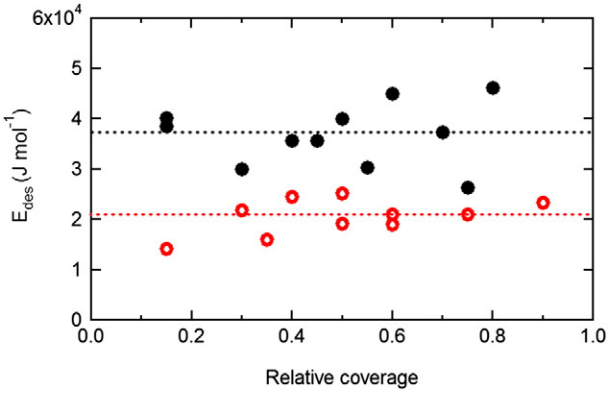


**Fig. 3.** CO desorption energies as a function of relative coverage for α (solid symbols) and $\beta_1$ (open symbols). Dashed lines indicate averages.

**Table 1**
Comparison of CO desorption energies for Au(310).

| | $E_{des}$ (α) kJ mol$^{-1}$ | $E_{des}$ ($\beta_1$) kJ mol$^{-1}$ |
|---|---|---|
| Current research *Red Head analysis* | 54 | 37 |
| Current research *complete analysis* | 37 ± 5 | 21 ± 3 |
| Weststrate et al. Ref. [23] | 46 ± 6 | 35 ± 4 |
| Hussain et al. Ref. [31] | 70 | – |

crystal surface were performed on Au(110) [34] and Au(111)[35]. For Au(111), a single desorption feature appears near 150 K which exhibits zeroth-order desorption kinetics. It was interpreted to indicate formation of 3-dimensional clusters at low coverage and, therefore, that this surface is hydrophobic [12,34]. STM studies have shown that initial adsorption occurs in 2-dimensional islands [36]. Outka and Madix reported two very closely spaced peak temperatures in TPD spectra of $H_2O$ desorbing from Au(110) at 185 and 190 K [34]. These results are not consistent with related systems, such as Ag(110) and Cu(110), and desorption temperatures near 200 K mostly occur when OH–$H_2O$ coadsorbed layers are formed from reaction with pre-adsorbed O or from electron-induced dissociation [16,17].

Our TPD spectra suggest two different adsorption states for water. The peak desorption temperature of the feature appearing at the lowest $H_2O$ doses shifts from 158 K to 172 K. The overlapping leading edges indicate zeroth-order desorption kinetics. Prior to saturation, a second desorption feature appears initially as a shoulder at ~165 K. This feature does not saturate even at very large $H_2O$ doses (not shown here). When closely examining the TPD traces for these higher $H_2O$ doses, we again observe a series of overlapping leading edges but starting near 150 K and exhibiting a steeper onset than those for the higher temperature feature. As water is generally found to initially bind to defects and step edges on other metals that do not dissociate water [17,37], it seems likely that the higher temperature feature in our spectra results from an adsorption state associated with the 6-fold coordinated Au atoms. A recent DFT study of water adsorption on Au(321), which contains similar 6-fold coordinated Au atoms in the step edge, also find these to be the most favorable adsorption sites [38]. The binding energy for a single $H_2O$ molecule is calculated to be 23 kJ/mol, whereas adsorption at the (111) terrace is less than10 kJ/mol. The resemblance of the lower temperature feature in our spectra to desorption from multilayers or clusters suggests that water only forms 2- or 3-dimensional structures after adsorption at step edges has nearly saturated. The zeroth-order desorption kinetics for $H_2O$ bound to step edges is somewhat surprising, as it does not occur on, for example, the (110) and (100) steps of Pt surfaces [37]. However, it is not uncommon to observe zeroth-order desorption kinetics in water desorption from (sub)monolayer coverages. It may result from, for example, the coexistence of a two-phase system on the surface at thermodynamic equilibrium [39].

The inset in Fig. 4 shows small changes in the desorption spectrum that occur when electrons are allowed to impinge from the QMS filament prior to and during the temperature ramp. Quiller et al. have also noticed that $H_2O$ on Au(111) is affected by electron impact [14]. In general, electrons may cause electron stimulated desorption (ESD) of water and dissociative electron attachment (DEA), where the latter has been used to generate OH groups on various metal surfaces that do not dissociate water [16]. We have recently done the same to study OH groups on Ni(111) [40]. We expect that the small changes observed in the TPD spectra in the inset of Fig. 4 result from a minor amount of water decomposition and, consequently, formation of O or OH within the $H_2O$ layer adsorbed to Au(310) surface. We have attempted to identify $H_2$ formation during electron irradiation but find no measurable increase in the partial pressure of m/z = 2 during electron irradiation.

### 3.3. Desorption of coadsorbed CO and $H_2O$ from Au(310)

To study coadsorption of $H_2O$ and CO, the Au(310) surface was consecutively exposed to $^{13}CO$ and $H_2O$. The amount of CO corresponds to a coverage of approximately 25% of the α feature shown in Fig. 2a. For the TPD traces shown in Fig. 5a ($H_2O$) and b (CO), the Au sample was kept at a negative bias of −49 V during dosing and measuring to prevent electron-induced reactions. Traces for increasing amounts of $H_2O$ show two interesting changes in comparison to desorption of the pure adsorbates. First, with increasing dose of $H_2O$,

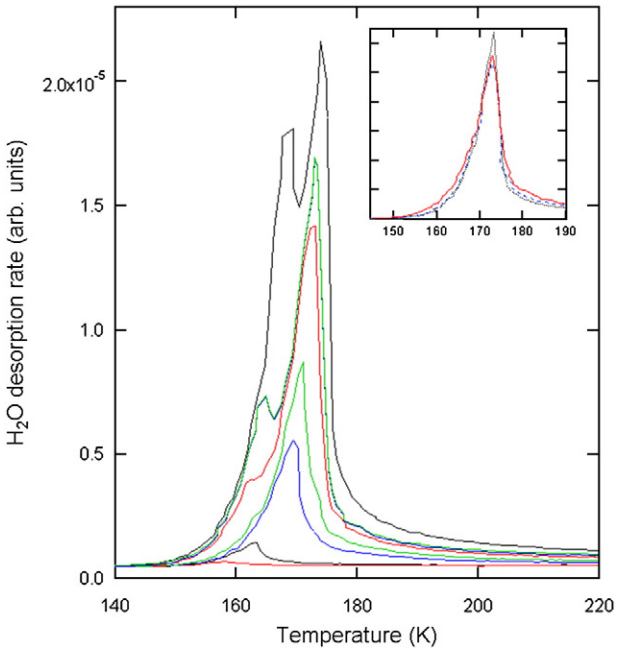


**Fig. 4.** $H_2O$ TPD spectra of various $H_2O$ doses. (inset) Spectra with 0.25 μA electron impact up to 49 V for 0 (dotted) 120 s (dashed) and 600 s (solid).

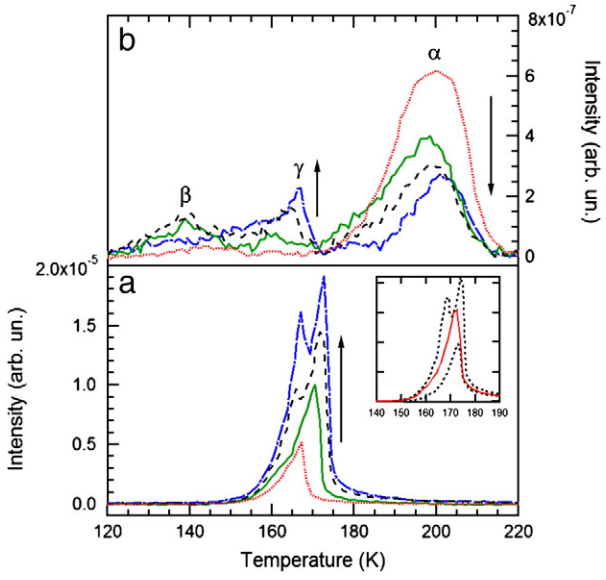


**Fig. 5.** TPD spectra of (a) $H_2O$ and (b) $^{13}CO$ for coadsorption with a fixed CO coverage and varying $H_2O$ coverage. The inset in (a) compares $H_2O$ desorption with (solid) and without (dashed) coadsorbed CO.

the amount of CO desorbing in α is reduced while more CO desorbs prior to $H_2O$. Second, in between α and $\beta_1$, we observe a third feature at ~165 K that increases with $H_2O$ exposure and occurs simultaneously with the lower temperature desorption feature of $H_2O$. It is labeled γ in Fig. 5b. The first observation indicates that $H_2O$ displaces some CO from step edge desorption sites. It is consistent with our interpretation of the high desorption feature in Fig. 4 as resulting from the step edge. Competition between $H_2O$ and CO for these sites may, e.g., lead to compression of CO adsorbed along the step edge, resulting in the appearance of the $\beta_1$ feature at such low CO coverages. The unchanged desorption temperature of $\beta_1$ tells us that there is little interaction between CO appearing in this feature and $H_2O$. The second observation, however, indicates that $H_2O$ and CO do interact at other locations and were likely bound very close to each other. Such $H_2O$–CO interaction does not result in CO oxidation, as no $CO_2$ was observed in any of these TPD experiments.

A more subtle change in the $H_2O$ desorption spectra is shown in the inset of Fig. 5a. We observe that pre-dosing CO affects the adsorption states of $H_2O$. The leading edge of the $H_2O$ TPD trace initially tracks desorption of the more weakly bound $H_2O$, but shifts toward the trace from the more strongly bound $H_2O$ as CO desorption in γ stops.

Fig. 6 shows an example of how electron irradiation changes TPD features for CO (Fig. 6a), $H_2O$ (Fig. 6b) and $CO_2$ (Fig. 6c). Dashed traces show desorption when the sample was kept at −49 V. For the solid traces, the sample was not biased during the TPD ramp and a 0.25 μA current impinged onto the $H_2O$/CO/Au(310) surface through the hole in the QMS's differentially pumped housing. We estimate that the e-flux was ~2 electrons per Au atom, based on the aperture, the current to the Au crystal and the time passed prior to $H_2O$ desorption (~100 s). Note that the slight variation in the total amount of CO desorption results from previously mentioned limited accuracy in dosing small amounts of CO.

The most prominent difference observed in Fig. 6 is the $^{13}CO_2$ production when electron irradiation is used. The $H_2O$ desorption trace is affected in the same way as shown in the inset of Fig. 4. This change may be expected if electron-induced dissociation results in dissociation of (part of) the adsorbed $H_2O$ molecules and formation of an OH–$H_2O$ network. Furthermore, we have verified that a decrease in $H_2O$ exposure with a fixed consecutive total electron flux leads to a decrease in $^{13}CO_2$ formation. Finally, $^{13}CO_2$ is only observed in the presence of both $H_2O$ and electron impact. Therefore, we can safely conclude that $^{13}CO$ oxidation results from products produced by electron impact on $H_2O$. We expect this to be surface-bound OH or O.

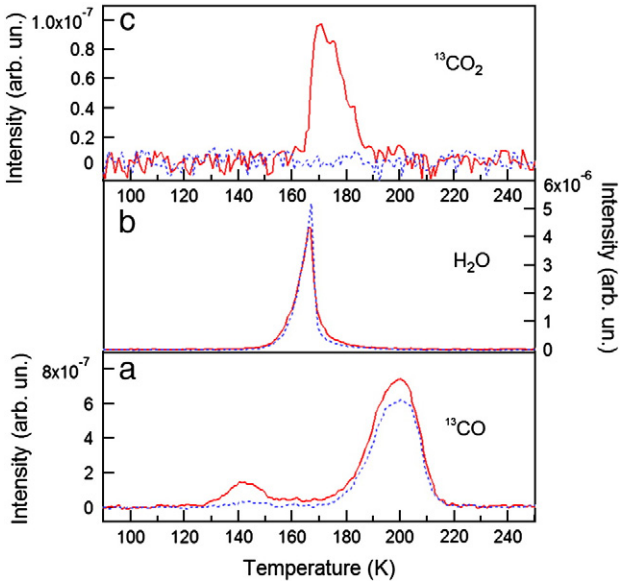


**Fig. 6.** TPD spectra of (a) $^{13}CO$ (b) $H_2O$ and (c) $^{13}CO_2$ for coadsorbed $^{13}CO$ and $H_2O$ without (dashed) and with (solid) electron irradiation.

Finally, the very steep onset of $CO_2$ production in Fig. 6 is noteworthy. $CO_2$ evolution suddenly starts at 164 K and continues in parallel with $H_2O$ desorption. This result is quite remarkable considering that CO was found to be oxidized by OH at a surface temperature of 77 K on Au(111) [12]. We consider two possible origins for this large difference in temperature. First, we consider possible differences in binding energies and activation barriers for CO oxidation. Falsig et al. have used DFT calculations to investigate CO oxidation on Au(111) and 12-atom Au clusters [41]. They find no barrier for the CO + O reaction at the Au(111) terrace. When using Au clusters, both the adsorption energy and transition state energy for CO + O drop by ~1 eV, thus yielding no significant activation barrier for CO oxidation at low coordinated Au atoms. Unless the stronger CO–Au bond on Au(310) entirely prohibits CO diffusion below ~160 K and both reactants are fully segregated at the surface, the reaction temperature difference cannot be explained by the variations in adsorption energies and activation barriers. Both of these requirements seem improbable as DFT-based calculations indicate small differences between the binding energies at various adsorption sites on Au(310) [31] and the γ feature in Fig. 5 strongly suggests interaction between $H_2O$ and CO on the surface. Second, we consider differences in the local O and OH environments. Results from experiments by Ojifinni et al. were performed mostly at rather low OH coverages created from reaction of isotopically labeled O with post-adsorbed $H_2O$. At 77 K, a molecular beam of CO reacted with (part of) the OH and left some O and CO on the surface. In our experiments, O or OH are most likely formed by electron irradiation within the hydrogen bonded network of $H_2O$ molecules. The $H_2O$ was dosed after CO adsorption and competes for step sites. As the CO oxidation appears during $H_2O$ desorption, we expect that O or OH only reacts with CO when the hydrating $H_2O$ network decomposes due to $H_2O$ desorption.

## 4. Summary

Using isotopic labeling, we have investigated desorption of CO and $H_2O$ from Au(310). Applying both Redhead and complete analyses to CO desorption spectra, we find strongly varying CO desorption energies. Both are substantially lower than those predicted by DFT calculations. TPD features for $H_2O$ desorption suggest two adsorption states on Au(310). We attribute the adsorption state with higher binding energy to step edge bound $H_2O$. Changes in $H_2O$ desorption spectra when using electron irradiation suggest dissociation of $H_2O$. This interpretation is corroborated by CO oxidation when we irradiate coadsorbed CO and $H_2O$ with electrons. Without electron irradiation, no $CO_2$ is formed. CO oxidation by fragments of $H_2O$ on Au(310) occurs at much higher temperatures than on Au(111). The difference is attributed to a hydration shell surrounding O or OH groups, making CO oxidation impossible until the excess water has desorbed.

## Acknowledgements

The authors kindly acknowledge the Leiden Institute of Chemistry for funding and Prof. Dr. Ben Nieuwenhuys for generous donation of equipment.

## References

[1] G.C. Bond, Gold Bulletin 5 (1972) 11.
[2] M. Haruta, T. Kobayashi, N. Yamada, Chemical Letters 2 (1987) 405.
[3] M. Haruta, Catalysis Today 36 (1997) 153.
[4] G.C. Bond, D.T. Thompson, Catalysis Reviews Science and Engineering 41 (1999) 319.
[5] R. Meyer, C. Lemire, Sh.K. Shaikhutdinov, H.-J. Freund, Gold Bulletin 37 (2004) 72.
[6] C.W. Corti, R.J. Holliday, D.T. Thompson, Topics in Catalysis 44 (2007) 331.

[7] B.K. Min, C.M. Friend, Chemical Reviews 107 (2007) 2709.
[8] J.L. Gong, C.B. Mullins, Accounts of Chemical Research 42 (2009) 1063.
[9] S.A.C. Carabineiro, B.E. Nieuwenhuys, Gold Bulletin 42 (2009) 288.
[10] S.A.C. Carabineiro, B.E. Nieuwenhuys, Gold Bulletin 43 (2010) 252.
[11] M. Daté, M. Okumura, S. Tsubota, M. Haruta, Angewandte Chemie, International Edition 43 (2004) 2129.
[12] R.A. Ojifinni, N.S. Froemming, J. Gong, M. Pan, T.S. Kim, J.M. White, G. Henkelman, C.B. Mullins, Journal of the American Chemical Society 130 (2008) 6801.
[13] S.D. Senanayake, D. Stacchiola, P. Liu, C.B. Mullins, J. Hrbek, J.A. Rodriguez, Journal of Physical Chemistry C 113 (2009) 19536.
[14] R.G. Quiller, T.A. Baker, X. Deng, M.E. Colling, B.K. Min, C.M. Friend, The Journal of Chemical Physics 129 (2008) 064702.
[15] P.A. Thiel, T.E. Madey, Surface Science Reports 7 (1987) 211.
[16] M.A. Henderson, Surface Science Reports 46 (2002) 5.
[17] A. Hodgson, S. Haq, Surface Science Reports 64 (2009) 381.
[18] M.J.T.C. van der Niet, A. en Dunnen, L.B.F. Juurlink, M.T.M. Koper, Angewandte Chemie, International Edition 49 (2010) 6572.
[19] Y.T. Yates Jr., first, Experimental Innovations in Surface Science, AIP Press, 1997, p. 572.
[20] D. Fargues, P. Dolle, J.J. Ehrhardt, M. Sotto, J.C. Boulliard, Surface Science 274 (1992) L495.
[21] M.A. van Hove, G.A. Somorjai, Surface Science 92 (1980) 489.
[22] Y.T. Yates Jr., Experimental Innovations in Surface Science, first, AIP Press, 1997, p. 604.
[23] C.J. Weststrate, E. Lundgren, J.N. Andersen, E.D.L. Rienks, A.C. Gluhoi, J.W. Bakker, I.M.N. Groot, B.E. Nieuwenhuys, Surface Science 603 (2009) 2152.
[24] C. Ruggiero, P. Hollins, Journal of the Chemical Society—Faraday Transactions 92 (1996) 4829.
[25] J. Kim, E. Samano, B.E. Koel, The Journal of Physical Chemistry. B 110 (2006) 17512.
[26] J.M. Gottfried, K.J. Schmidt, S.L.M. Schroeder, K. Christmann, Surface Science 536 (2003) 206.
[27] W.-L. Yim, T. Nowitzki, M. Necke, H. Schnars, P. Nickut, J. Biener, M.M. Biener, V. Zielasek, K. Al-Shamery, T. Klüner, M. Bäumer, Journal of Chemical Physics C 111 (2007) 445.
[28] P.A. Redhead, Vacuum 12 (1962) 203.
[29] D.A. King, Surface Science 47 (1975) 384.
[30] A.M. de Jong, J.W. Niemantsverdriet, Surface Science 233 (1990) 355.
[31] A. Hussain, D.C. Ferré, J. Gracia, B.E. Nieuwenhuys, J.W. Niemantsverdriet, Surface Science 603 (2009) 2734.
[32] N. Lopez, T.V.W. Janssens, B.S. Clausen, Y. Xu, M. Mavrikakis, T. Bligaard, J.K. Nørskov, Journal of Catalysis 223 (2004) 232.
[33] J.L.C. Fajín, M.N.D.S. Cordeiro, J.R.B. Gomes, Journal of Physical Chemistry C 112 (2008) 17291.
[34] D.A. Outka, R.J. Madix, Journal of the American Chemical Society 109 (1987) 1708.
[35] B.D. Kay, K.R. Lykke, J.R. Creighton, S.J. Ward, The Journal of Chemical Physics 91 (1989) 5120.
[36] N. Ikemiya, A.A. Gewirth, Journal of the American Chemical Society 119 (1997) 9919.
[37] M.J.T.C. van der Niet, A. den Dunnen, L.B.F. Juurlink, M.T.M. Koper, The Journal of Chemical Physics 132 (2010) 174705.
[38] J.L. Fajín, M.N.D.S. Cordeiro, J.R.B. Gomes, Journal of Molecular Structure: THEOCHEM 946 (2010) 51.
[39] J.L. Daschbach, B.M. Peden, R.S. Smith, B.D. Kay, The Journal of Chemical Physics 120 (2004) 1516.
[40] J. Shan, A.W. Kleyn, L.B.F. Juurlink, ChemPhysChem 10 (2009) 270.
[41] H. Falsig, B. Hvolbæk, I.S. Kristensen, T. Jiang, T. Bligaard, C.H. Christensen, J.K. Nørskov, Angewandte Chemie, International Edition 47 (2008) 4835.